

Observation of two resonance-like structures in the $\pi^+\chi_{c1}$ mass distribution in exclusive $\bar{B}^0 \rightarrow K^-\pi^+\chi_{c1}$ decays

R. Mizuk,¹³ R. Chistov,¹³ I. Adachi,⁹ H. Aihara,⁴⁰ K. Arinstein,¹ V. Aulchenko,¹ T. Aushev,^{18,13} A. M. Bakich,³⁷ V. Balagura,¹³ E. Barberio,²¹ A. Bay,¹⁸ V. Bhardwaj,³² U. Bitenc,¹⁴ A. Bondar,¹ A. Bozek,²⁷ M. Bračko,^{20,14} J. Brodzicka,⁹ T. E. Browder,⁸ M.-C. Chang,³ P. Chang,²⁶ A. Chen,²⁴ K.-F. Chen,²⁶ B. G. Cheon,⁷ C.-C. Chiang,²⁶ I.-S. Cho,⁴⁵ S.-K. Choi,⁶ Y. Choi,³⁶ J. Dalseno,⁹ M. Danilov,¹³ A. Drutskoy,² S. Eidelman,¹ D. Epifanov,¹ P. Goldenzweig,² B. Golob,^{19,14} H. Ha,¹⁶ J. Haba,⁹ K. Hayasaka,²² H. Hayashii,²³ M. Hazumi,⁹ Y. Hoshi,³⁹ W.-S. Hou,²⁶ Y. B. Hsiung,²⁶ H. J. Hyun,¹⁷ T. Iijima,²² K. Inami,²² A. Ishikawa,³³ H. Ishino,⁴¹ R. Itoh,⁹ M. Iwasaki,⁴⁰ Y. Iwasaki,⁹ D. H. Kah,¹⁷ H. Kaji,²² J. H. Kang,⁴⁵ T. Kawasaki,²⁹ H. Kichimi,⁹ H. J. Kim,¹⁷ H. O. Kim,¹⁷ Y. I. Kim,¹⁷ Y. J. Kim,⁵ K. Kinoshita,² S. Korpar,^{20,14} P. Križan,^{19,14} P. Krokovny,⁹ R. Kumar,³² A. Kuzmin,¹ Y.-J. Kwon,⁴⁵ S.-H. Kyeong,⁴⁵ J. S. Lange,⁴ J. S. Lee,³⁶ M. J. Lee,³⁵ S.-W. Lin,²⁶ C. Liu,³⁴ Y. Liu,⁵ D. Liventsev,¹³ F. Mandl,¹¹ S. McOnie,³⁷ K. Miyabayashi,²³ H. Miyata,²⁹ Y. Miyazaki,²² E. Nakano,³¹ M. Nakao,⁹ H. Nakazawa,²⁴ S. Nishida,⁹ O. Nitoh,⁴³ S. Ogawa,³⁸ T. Ohshima,²² S. Okuno,¹⁵ S. L. Olsen,^{8,10} H. Ozaki,⁹ P. Pakhlov,¹³ G. Pakhlova,¹³ H. Palka,²⁷ C. W. Park,³⁶ H. Park,¹⁷ H. K. Park,¹⁷ L. S. Peak,³⁷ R. Pestotnik,¹⁴ L. E. Piilonen,⁴⁴ A. Poluektov,¹ H. Sahoo,⁸ Y. Sakai,⁹ O. Schneider,¹⁸ A. J. Schwartz,² K. Senyo,²² J.-G. Shiu,²⁶ B. Shwartz,¹ J. B. Singh,³² A. Sokolov,¹² A. Somov,² S. Stanič,³⁰ M. Starič,¹⁴ T. Sumiyoshi,⁴² M. Tanaka,⁹ G. N. Taylor,²¹ Y. Teramoto,³¹ I. Tikhomirov,¹³ K. Trabelsi,⁹ S. Uehara,⁹ T. Uglov,¹³ Y. Unno,⁷ S. Uno,⁹ P. Urquijo,²¹ Y. Usov,¹ G. Varner,⁸ K. E. Varvell,³⁷ K. Vervink,¹⁸ C. H. Wang,²⁵ M.-Z. Wang,²⁶ P. Wang,¹⁰ X. L. Wang,¹⁰ Y. Watanabe,¹⁵ J. Wicht,⁹ E. Won,¹⁶ B. D. Yabsley,³⁷ Y. Yamashita,²⁸ C. C. Zhang,¹⁰ Z. P. Zhang,³⁴ V. Zhilich,¹ V. Zhulanov,¹ T. Zivko,¹⁴ A. Zupanc,¹⁴ and O. Zyukova¹

(The Belle Collaboration)

¹*Budker Institute of Nuclear Physics, Novosibirsk*

²*University of Cincinnati, Cincinnati, Ohio 45221*

³*Department of Physics, Fu Jen Catholic University, Taipei*

⁴*Justus-Liebig-Universität Gießen, Gießen*

⁵*The Graduate University for Advanced Studies, Hayama*

⁶*Gyeongsang National University, Chinju*

⁷*Hanyang University, Seoul*

⁸*University of Hawaii, Honolulu, Hawaii 96822*

⁹*High Energy Accelerator Research Organization (KEK), Tsukuba*

¹⁰*Institute of High Energy Physics, Chinese Academy of Sciences, Beijing*

¹¹*Institute of High Energy Physics, Vienna*

¹²*Institute of High Energy Physics, Protvino*

¹³*Institute for Theoretical and Experimental Physics, Moscow*

¹⁴*J. Stefan Institute, Ljubljana*

¹⁵*Kanagawa University, Yokohama*

¹⁶*Korea University, Seoul*

¹⁷*Kyungpook National University, Taegu*

¹⁸*École Polytechnique Fédérale de Lausanne (EPFL), Lausanne*

¹⁹*Faculty of Mathematics and Physics, University of Ljubljana, Ljubljana*

²⁰*University of Maribor, Maribor*

²¹*University of Melbourne, School of Physics, Victoria 3010*

²²*Nagoya University, Nagoya*

²³*Nara Women's University, Nara*

²⁴*National Central University, Chung-li*

²⁵*National United University, Miao Li*

²⁶*Department of Physics, National Taiwan University, Taipei*

²⁷*H. Niewodniczanski Institute of Nuclear Physics, Krakow*

²⁸*Nippon Dental University, Niigata*

²⁹*Niigata University, Niigata*

³⁰*University of Nova Gorica, Nova Gorica*

³¹*Osaka City University, Osaka*

³²*Panjab University, Chandigarh*

³³*Saga University, Saga*

³⁴University of Science and Technology of China, Hefei

³⁵Seoul National University, Seoul

³⁶Sungkyunkwan University, Suwon

³⁷University of Sydney, Sydney, New South Wales

³⁸Toho University, Funabashi

³⁹Tohoku Gakuin University, Tagajo

⁴⁰Department of Physics, University of Tokyo, Tokyo

⁴¹Tokyo Institute of Technology, Tokyo

⁴²Tokyo Metropolitan University, Tokyo

⁴³Tokyo University of Agriculture and Technology, Tokyo

⁴⁴Virginia Polytechnic Institute and State University, Blacksburg, Virginia 24061

⁴⁵Yonsei University, Seoul

We report the first observation of two resonance-like structures in the $\pi^+\chi_{c1}$ invariant mass distribution near $4.1\text{ GeV}/c^2$ in exclusive $\bar{B}^0 \rightarrow K^-\pi^+\chi_{c1}$ decays. From a Dalitz plot analysis in which the $\pi^+\chi_{c1}$ mass structures are represented by Breit-Wigner resonance amplitudes, we determine masses and widths of: $M_1 = (4051 \pm 14^{+20}_{-41})\text{ MeV}/c^2$, $\Gamma_1 = (82^{+21+47}_{-17-22})\text{ MeV}$, $M_2 = (4248^{+44+180}_{-29-35})\text{ MeV}/c^2$, and $\Gamma_2 = (177^{+54+316}_{-39-61})\text{ MeV}$; and product branching fractions of $\mathcal{B}(\bar{B}^0 \rightarrow K^-Z_{1,2}^+) \times \mathcal{B}(Z_{1,2}^+ \rightarrow \pi^+\chi_{c1}) = (3.0^{+1.5+3.7}_{-0.8-1.6}) \times 10^{-5}$ and $(4.0^{+2.3+19.7}_{-0.9-0.5}) \times 10^{-5}$ respectively. Here the first uncertainty is statistical, the second is systematic. The significance of each of the $\pi^+\chi_{c1}$ structures exceeds 5σ , including the systematic uncertainty from various fit models. This analysis is based on 657×10^6 $B\bar{B}$ events collected at the $\Upsilon(4S)$ resonance with the Belle detector at the KEKB asymmetric-energy e^+e^- collider.

PACS numbers: 14.40.Gx, 12.39.Mk, 13.25.Hw

INTRODUCTION

Recently the Belle Collaboration reported the observation of a relatively narrow resonance-like structure in the $\pi^+\psi(2S)$ mass spectrum produced in $\bar{B}^0 \rightarrow K^-\pi^+\psi(2S)$ decays, calling this structure the $Z(4430)^+$ [1]. If the $Z(4430)^+$ is interpreted as a meson state, then its minimal quark content must be the exotic combination $|c\bar{c}u\bar{d}\rangle$. The $Z(4430)^+$ observation motivated studies of other $\bar{B}^0 \rightarrow K^-\pi^+(c\bar{c})$ decays.

In this paper we present a study of the decay $\bar{B}^0 \rightarrow K^-\pi^+\chi_{c1}$, including the first observation of a doubly peaked structure in the $\pi^+\chi_{c1}$ invariant mass distribution near $4.1\text{ GeV}/c^2$. If the two peaks are meson states, their minimal quark content must be the same as that of the $Z(4430)^+$. The analysis is performed using data collected with the Belle detector at the KEKB asymmetric-energy e^+e^- collider [2]. The data sample consists of 605 fb^{-1} accumulated at the $\Upsilon(4S)$ resonance, which corresponds to 657×10^6 $B\bar{B}$ pairs.

BELLE DETECTOR

The Belle detector is a large-solid-angle magnetic spectrometer that consists of a silicon vertex detector (SVD), a 50-layer central drift chamber (CDC), an array of aerogel threshold Cherenkov counters (ACC), a barrel-like arrangement of time-of-flight scintillation counters (TOF), and an electromagnetic calorimeter (ECL) comprising CsI(Tl) crystals located inside a superconducting solenoid coil that provides a 1.5 T magnetic field. An iron

flux-return located outside of the coil is instrumented to detect K_L^0 mesons and to identify muons (KLM). The detector is described in detail elsewhere [3]. Two different inner detector configurations were used, a 2.0 cm radius beam-pipe and a 3-layer silicon vertex detector for the first 155 fb^{-1} , and a 1.5 cm radius beam-pipe with a 4-layer vertex detector for the remaining 450 fb^{-1} [4].

We use a GEANT-based Monte Carlo (MC) simulation [5] to model the response of the detector, identify potential backgrounds and determine the acceptance. The MC simulation includes run-dependent detector performance variations and background conditions. Signal MC events are generated in proportion to the relative luminosities of the different running periods.

EVENT SELECTION

We select events of the type $\bar{B}^0 \rightarrow K^-\pi^+\chi_{c1}$, where the χ_{c1} meson is reconstructed via its decay to $J/\psi\gamma$, with a subsequent J/ψ decay to $\ell^+\ell^-$ ($\ell^+\ell^- = e^+e^-$ or $\mu^+\mu^-$). The inclusion of charge-conjugate modes is implied throughout this paper.

All tracks are required to originate from the beam-beam interaction region: $dr < 0.2\text{ cm}$ and $dz < 2\text{ cm}$, where dr is the distance of closest approach to the beam-beam interaction point in the plane perpendicular to the beam axis and dz is the corresponding distance along the beam direction. Charged pions and kaons are identified using a likelihood ratio method that combines information from the TOF system and ACC counters with energy loss (dE/dx) measurements from the CDC. The identifi-

cation requirements for kaons have an efficiency of 90% and a pion misidentification probability of 10%. Muons are identified by their range and transverse scattering in the KLM. Electrons are identified by the presence of a matching ECL cluster with transverse energy profile consistent with an electromagnetic shower. In addition, charged pions and kaons that are also positively identified as electrons are rejected.

Photons are identified as energy clusters in the ECL that have no associated charged tracks detected in the CDC, and a shower shape that is consistent with that of a photon.

For $J/\psi \rightarrow e^+e^-$ candidates, photons that have laboratory frame energies greater than 30 MeV and are within 50 mrad of the direction of the e^+ or e^- tracks are included in the invariant mass calculation; we require $|M(e^+e^-) - m_{J/\psi}| < 50 \text{ MeV}/c^2$. For $J/\psi \rightarrow \mu^+\mu^-$ candidates we require $|M(\mu^+\mu^-) - m_{J/\psi}| < 30 \text{ MeV}/c^2$. To enhance the precision of the J/ψ energy and momentum determination, we perform a mass constrained fit to the J/ψ candidates.

For $\chi_{c1} \rightarrow J/\psi\gamma$ candidates, we use photons with laboratory frame energies greater than 50 MeV and require $|M(J/\psi\gamma) - m_{\chi_{c1}}| < 30 \text{ MeV}/c^2$. To improve the accuracy of the χ_{c1} energy and momentum determination, we perform a mass constrained fit to the χ_{c1} candidates.

Candidate $\bar{B}^0 \rightarrow K^-\pi^+\chi_{c1}$ decays are identified by their center-of-mass (c.m.) energy difference, $\Delta E = \sum_i E_i - E_{\text{beam}}$, and their beam-energy constrained mass, $M_{\text{bc}} = \sqrt{E_{\text{beam}}^2 - (\sum_i \vec{p}_i)^2}$, where $E_{\text{beam}} = \sqrt{s}/2$ is the beam energy in the c.m. and \vec{p}_i and E_i are the three-momenta and energies of the B candidate's decay products. We accept B candidates with $5275 \text{ MeV}/c^2 < M_{\text{bc}} < 5287 \text{ MeV}/c^2$ and $|\Delta E| < 12 \text{ MeV}$. The ΔE sidebands are defined as $24 \text{ MeV} < |\Delta E| < 96 \text{ MeV}$. To have well defined Dalitz plot boundaries for both signal and sideband events, we perform a mass constrained fit to the \bar{B}^0 candidates from both regions (to the nominal \bar{B}^0 mass in all cases).

ANALYSIS OF $\bar{B}^0 \rightarrow K^-\pi^+\chi_{c1}$ DECAYS

The ΔE distribution for selected $\bar{B}^0 \rightarrow K^-\pi^+\chi_{c1}$ candidates is shown in Fig. 1. The contribution of the χ_{c1} sideband regions defined as $140 \text{ MeV}/c^2 < |M(J/\psi\gamma) - m_{\chi_{c1}}| < 230 \text{ MeV}/c^2$ is also shown. The χ_{c1} sidebands account for almost all the background, which indicates that the background is primarily due to combinatorial photons; the contamination from events with misidentified particles is found to be negligibly small. The $M(J/\psi\gamma)$ distributions before the χ_{c1} mass constrained fit for the ΔE signal and sideband regions are shown in Fig. 2. There is a small χ_{c1} signal in the ΔE sidebands due to inclusive χ_{c1} production in B decays. The J/ψ signals in the $M(\mu^+\mu^-)$ and $M(e^+e^-)$ distributions are

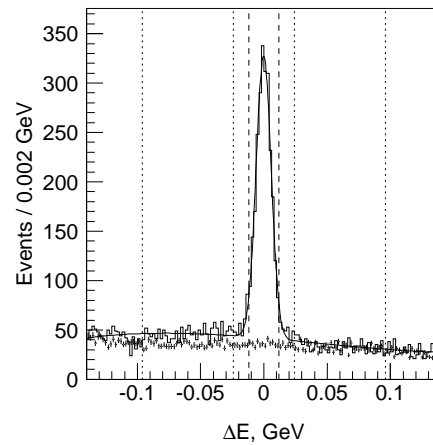


FIG. 1: The ΔE distribution for the selected \bar{B}^0 meson candidates (histogram) and for the χ_{c1} sidebands (points with error bars). The vertical lines indicate the ΔE signal and sideband regions.

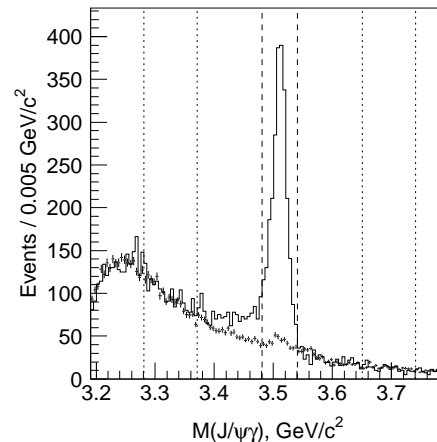


FIG. 2: The $M(J/\psi\gamma)$ distribution for the selected \bar{B}^0 meson candidates (histogram) and for the ΔE sidebands (points with error bars). The vertical lines indicate the χ_{c1} signal and sideband regions.

almost background-free.

A signal yield of $2126 \pm 56 \pm 42$ $\bar{B}^0 \rightarrow K^-\pi^+\chi_{c1}$ events is determined from a fit to the ΔE distribution using a Gaussian function to represent the signal plus a second-order polynomial to represent the background. The fitted ΔE resolution, $\sigma = (5.93 \pm 0.15 \pm 0.13) \text{ MeV}/c^2$, is consistent with the MC expectation of $\sigma = (5.62 \pm 0.03 \pm 0.09) \text{ MeV}/c^2$. Here and elsewhere in this report the first uncertainty is statistical, the second is systematic. The systematic uncertainties for the signal yield and the ΔE width are estimated by varying the ΔE interval covered by the fit.

To determine the detection efficiency, we simulate $B^0\bar{B}^0$ events where $\bar{B}^0 \rightarrow K^-\pi^+\chi_{c1}$ with a uniform phase-space distribution and the accompanying B^0 de-

cays generically. These MC events are then weighted according to the results of the fit to the Dalitz plot that is described below. In this way, the reconstruction efficiency is found to be $(20.0 \pm 1.4)\%$, where the following sources are included in the uncertainty: the dependence on the Dalitz plot model (0.2%); data and MC differences for track and γ reconstruction ($1\% \times 4$ for four tracks and 1.5% for γ), and particle identification (4% for the $K^- \pi^+$ pair and 4.2% for $\ell^+ \ell^-$); uncertainties in the angular distributions for $\chi_{c1} \rightarrow J/\psi \gamma$ and $J/\psi \rightarrow \ell^+ \ell^-$ decays (0.2%); and MC statistics (0.6%). The uncertainties from different sources are added in quadrature. The efficiency is corrected for the difference in lepton identification performance in data compared to MC, $(-4.5 \pm 4.2)\%$, as estimated from $J/\psi \rightarrow \ell^+ \ell^-$ and $e^+ e^- \rightarrow e^+ e^- \ell^+ \ell^-$ control samples.

Using $(656.7 \pm 8.9) \times 10^6$ as the number of $B\bar{B}$ pairs and Particle Data Group (PDG) 2006 values for the branching fractions $\mathcal{B}(\chi_{c1} \rightarrow J/\psi \gamma) = 0.356 \pm 0.019$ and $\mathcal{B}(J/\psi \rightarrow \ell^+ \ell^-) = 0.1187 \pm 0.0012$ [6], we determine

$$\mathcal{B}(\bar{B}^0 \rightarrow K^- \pi^+ \chi_{c1}) = (3.83 \pm 0.10 \pm 0.39) \times 10^{-4}.$$

The systematic uncertainty includes contributions from the uncertainty in the efficiency (7.2%), the systematic uncertainty in the signal yield (2.0%), the uncertainty due to the variation in the selection requirements (3.9%), the uncertainty in the ΔE signal shape (1.0%, considering a sum of two Gaussian functions instead of a single one) and the uncertainties in the χ_{c1} and J/ψ decay branching fractions (5.3% and 1.0%, respectively).

The $\bar{B}^0 \rightarrow K^- \pi^+ \chi_{c1}$ decay Dalitz plot ($M^2(\pi^+ \chi_{c1})$ versus $M^2(K^- \pi^+)$) for the ΔE signal region is shown in Fig. 3 (a). The Dalitz plot distribution exhibits some distinct features: a vertical band at $M^2(K^- \pi^+) \simeq 0.8 \text{ GeV}^2/c^4$ that corresponds to $\bar{B}^0 \rightarrow K^*(892) \chi_{c1}$ decays; a clustering of events at $M^2(K^- \pi^+) \simeq 2 \text{ GeV}^2/c^4$ that corresponds primarily to $\bar{B}^0 \rightarrow K^*(1430) \chi_{c1}$ decays; a distinct horizontal band at $M^2(\pi^+ \chi_{c1}) \simeq 17 \text{ GeV}^2/c^4$ corresponding to a structure in the $\pi^+ \chi_{c1}$ channel, denoted by Z^+ . This latter feature is the subject of this report.

In contrast, the Dalitz plot for the ΔE sidebands, shown in Fig. 3 (b), is relatively smooth and featureless. The Dalitz plot for the phase-space MC candidate events, shown in Fig. 4, also exhibits a smooth and featureless behaviour. There is a decrease in efficiency in the top (bottom) region where the K^- (π^+) is slow and has a low detection efficiency.

FORMALISM OF DALITZ ANALYSIS

The decay $\bar{B}^0 \rightarrow K^- \pi^+ \chi_{c1}$ with the χ_{c1} reconstructed in the $J/\psi \gamma$ decay mode and the J/ψ reconstructed in the $\ell^+ \ell^-$ decay mode is described by six variables (assuming

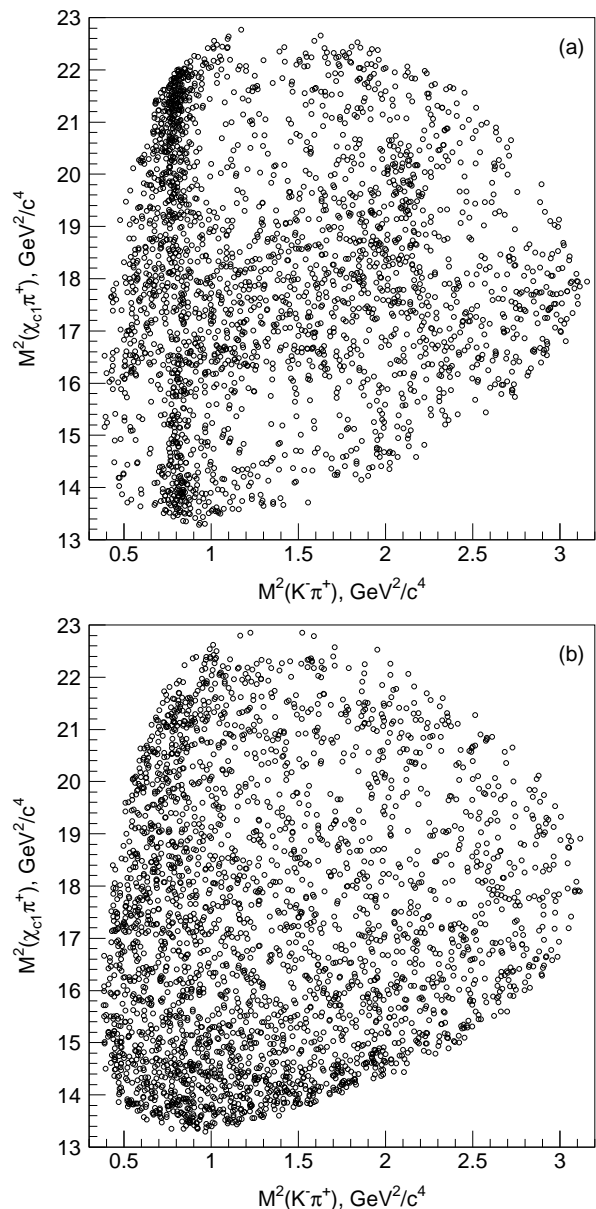


FIG. 3: The $\bar{B}^0 \rightarrow K^- \pi^+ \chi_{c1}$ decay Dalitz plot for the ΔE signal (a) and sideband (b) regions.

the widths of the χ_{c1} and J/ψ to be negligible). We take these to be $M(\pi^+ \chi_{c1})$, $M(K^- \pi^+)$, the χ_{c1} and J/ψ helicity angles ($\theta_{\chi_{c1}}$ and $\theta_{J/\psi}$), and the angle between the χ_{c1} (J/ψ) production and decay planes $\phi_{\chi_{c1}}$ ($\phi_{J/\psi}$). Here we analyze the $\bar{B}^0 \rightarrow K^- \pi^+ \chi_{c1}$ decay process after integrating over the angular variables $\theta_{\chi_{c1}}$, $\theta_{J/\psi}$, $\phi_{\chi_{c1}}$ and $\phi_{J/\psi}$. We find that the reconstruction efficiency is almost uniform over the full $\phi_{\chi_{c1}}$ and $\phi_{J/\psi}$ angular ranges; therefore, after integrating over these angles the interference terms between different χ_{c1} helicity states, which contain factors of $\sin \phi_{\chi_{c1}}$, $\cos \phi_{\chi_{c1}}$, $\sin 2\phi_{\chi_{c1}}$ or $\cos 2\phi_{\chi_{c1}}$, are negligibly small. We subsequently verify that the $\theta_{\chi_{c1}}$ and $\theta_{J/\psi}$ distributions agree with these expectations.

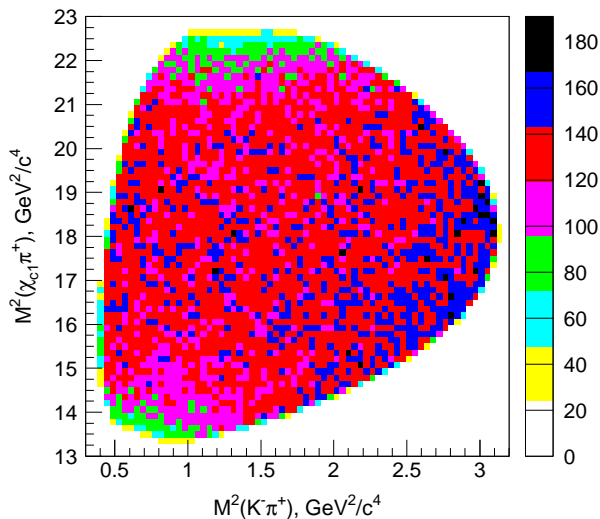


FIG. 4: Dalitz plot for reconstructed $\bar{B}^0 \rightarrow K^- \pi^+ \chi_{c1}$ MC events, generated according to the phase space model.

We perform a binned likelihood fit to the Dalitz plot distribution, where the bin size is chosen by decreasing its area until the fit results are unaffected by further changes. The selected number of bins is 400×400 . We consider only those bins that are fully contained within the Dalitz plot boundaries; this corresponds to 99.3% of the total Dalitz plot area.

In 1.9% of events from the ΔE signal region we find more than one \bar{B}^0 candidate. Multiple candidates are uniformly distributed over the entire Dalitz plot area. No best candidate selection is applied.

We use a fitting function of the form

$$F(s_x, s_y) = S(s_x, s_y) \times \epsilon(s_x, s_y) + B(s_x, s_y), \quad (1)$$

where $s_x \equiv M^2(K^- \pi^+)$, $s_y \equiv M^2(\pi^+ \chi_{c1})$, S and B are the signal and background event density functions, and ϵ is the detection efficiency. The background $B(s_x, s_y)$ is determined from the ΔE sidebands. Its normalization is allowed to float in the fit within its corresponding uncertainty. The bin-by-bin efficiency $\epsilon(s_x, s_y)$ is determined from the MC simulation. Both sidebands and efficiency distributions are smoothed.

The amplitude for the three-body decay $\bar{B}^0 \rightarrow K^- \pi^+ \chi_{c1}$ is represented as the sum of Breit-Wigner contributions for different intermediate two-body states. This type of description, which is widely used in high energy physics for Dalitz plot analyses [7], cannot be exact since it is neither unitary nor analytic and does not take into account a complete description of final state interactions. Nevertheless, the sum of Breit-Wigner terms reflects the main features of the amplitude's behaviour and provides a way to find and distinguish the contributions of the two-body intermediate states, their mutual interference, and their effective resonance parameters.

Our default fit model includes all known $K^- \pi^+$ resonances below $1900 \text{ MeV}/c^2$ (κ , $K^*(892)$, $K^*(1410)$, $K_0^*(1430)$, $K_2^*(1430)$, $K^*(1680)$, $K_3^*(1780)$) and a single exotic $\chi_{c1} \pi^+$ resonance. The amplitude for $\bar{B}^0 \rightarrow K^- \pi^+ \chi_{c1}$ via a two-body intermediate resonance R (R denotes either a $K^- \pi^+$ or $\pi^+ \chi_{c1}$ resonance) and the χ_{c1} meson in helicity state λ is given by

$$A_\lambda^R(s_x, s_y) = F_B^{(L_B)} \cdot \frac{1}{M_R^2 - s_R - iM_R \Gamma(s_R)} \cdot F_R^{(L_R)} \cdot T_\lambda \cdot \left(\frac{p_B}{m_B}\right)^{L_B} \cdot \left(\frac{p_R}{\sqrt{s_R}}\right)^{L_R}. \quad (2)$$

Here $F_B^{(L_B)}$ and $F_R^{(L_R)}$ are the \bar{B}^0 meson and R resonance decay form factors (the superscript denotes the orbital angular momentum of the decay); M_R is the resonance mass, s_R is the four-momentum-squared and $\Gamma(s_R)$ is the energy-dependent width of the R resonance; T_λ is the angle-dependent term; $\left(\frac{p_B}{m_B}\right)^{L_B} \cdot \left(\frac{p_R}{\sqrt{s_R}}\right)^{L_R}$ is a factor related to the momentum dependence of the wave function, p_B (p_R) is the \bar{B}^0 meson (R resonance) daughter's momentum in the B (R) rest frame; and m_B is the \bar{B}^0 meson mass.

We use the Blatt-Weisskopf form factors given in Ref. [8]:

$$\begin{aligned} F^{(0)} &= 1, \\ F^{(1)} &= \frac{\sqrt{1+z_0}}{\sqrt{1+z}}, \\ F^{(2)} &= \frac{\sqrt{z_0^2 + 3z_0 + 9}}{\sqrt{z^2 + 3z + 9}}, \\ F^{(3)} &= \frac{\sqrt{z_0^3 + 6z_0^2 + 45z_0 + 225}}{\sqrt{z^3 + 6z^2 + 45z + 225}}. \end{aligned} \quad (3)$$

Here $z = r^2 p_R^2$ where r is the hadron scale, taken to be $r = 1.6 (\text{GeV}/c)^{-1}$, and $z_0 = r^2 p_{R0}^2$ where p_{R0} is the R resonance daughter's momentum calculated for the pole mass of the R resonance. For K^* resonances with non-zero spin, the B decay orbital angular momentum L_B can take several values (S , P & D -waves for $J = 1$; P , D & F -waves for $J = 2$; and D , F & G -waves for $J = 3$). We take the lowest L_B as the default value and consider the other possibilities in the systematic uncertainty. The energy-dependent width is parameterized as

$$\Gamma(s_R) = \Gamma_0 \cdot (p_R/p_{R0})^{2L_R+1} \cdot (m_R/\sqrt{s_R}) \cdot F_R^2. \quad (4)$$

The angular function T_λ is obtained using the helicity formalism. For the $\bar{B}^0 \rightarrow K^*(\rightarrow K^- \pi^+) \chi_{c1}$ decay

$$T_\lambda = d_{\lambda 0}^J(\theta_{K^*}), \quad (5)$$

where J is the spin of the K^* resonance; θ_{K^*} is the helicity angle of the K^* decay. For the $\bar{B}^0 \rightarrow K^- Z^+(\rightarrow \pi^+ \chi_{c1})$ decay

$$T_\lambda = d_{\lambda 0}^J(\theta_{Z^+}), \quad (6)$$

where J is the spin of the Z^+ resonance and θ_{Z^+} is the helicity angle of the Z^+ decay.

In the decays $\bar{B}^0 \rightarrow K^*(\rightarrow K^-\pi^+)\chi_{c1}$ and $\bar{B}^0 \rightarrow K^-Z^+(\rightarrow \pi^+\chi_{c1})$ the parent particles of the χ_{c1} are different and, therefore, the relevant χ_{c1} helicity is defined relative to different axes: for $\bar{B}^0 \rightarrow K^*(\rightarrow K^-\pi^+)\chi_{c1}$ the axis is parallel to the $K^-\pi^+$ momentum in the χ_{c1} rest frame; for $\bar{B}^0 \rightarrow K^-Z^+(\rightarrow \pi^+\chi_{c1})$ the axis is parallel to the π^+ momentum in the χ_{c1} rest frame. The angle θ between the two axes depends upon the event's location in the Dalitz plot as indicated in Fig. 5. As a

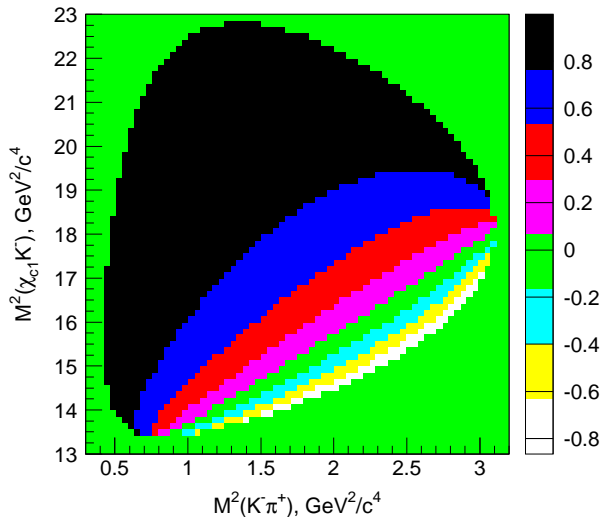


FIG. 5: $\cos\theta$ as a function of the Dalitz plot variables, where θ is the angle between the helicity axes for $K\pi$ and $\pi\chi_{c1}$ intermediate resonances.

result, the state $|\lambda\rangle_{Z^+}$ with χ_{c1} helicity λ produced in the decay $\bar{B}^0 \rightarrow K^-Z^+(\rightarrow \pi^+\chi_{c1})$ is not equal to the state $|\lambda\rangle_{K^*}$ with the same χ_{c1} helicity λ produced in the decay $\bar{B}^0 \rightarrow K^*(\rightarrow K^-\pi^+)\chi_{c1}$. The two states are related by the Wigner d -functions via

$$|\lambda\rangle_{K^*} = \sum_{\lambda'=-1,0,1} d_{\lambda'\lambda}^1(\theta) |\lambda'\rangle_{Z^+}; \quad (7)$$

the same relation holds for the amplitudes.

The resulting expression for the signal event density function is

$$S(s_x, s_y) = \sum_{\lambda=-1,0,1} \left| \sum_{K^*} a_{\lambda}^{K^*} e^{i\phi_{\lambda}^{K^*}} A_{\lambda}^{K^*}(s_x, s_y) + \sum_{\lambda'=-1,0,1} d_{\lambda'\lambda}^1(\theta) a_{\lambda'}^{Z^+} e^{i\phi_{\lambda'}^{Z^+}} A_{\lambda'}^{Z^+}(s_x, s_y) \right|^2, \quad (8)$$

where a_{λ}^R and ϕ_{λ}^R are the normalizations and phases of the amplitudes for the intermediate resonance R and χ_{c1} helicity λ . The phase $\phi_0^{K^*}$ (892) is fixed to zero. The detector resolution ($\sigma \sim 2 \text{ MeV}/c^2$) is small compared to

the width of any of the resonances that are considered and is ignored.

The masses and widths of the K^* resonances are fixed to their PDG values, except for the κ , for which the mass and width are allowed to vary within their experimental uncertainties [6]. The mass and width of the Z^+ is allowed to vary without any restrictions.

RESULTS

To display the results of the fit, we divide the Dalitz plot into four vertical and three horizontal slices as shown in Fig. 6. Projections of the fit results for the seven slices

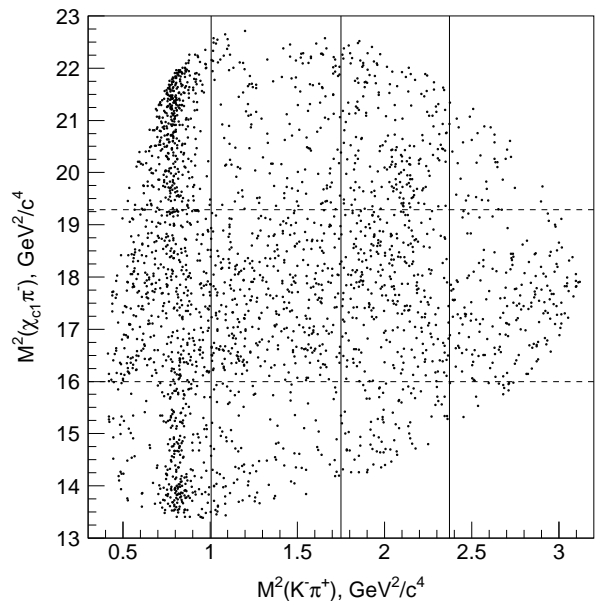


FIG. 6: The $\bar{B}^0 \rightarrow K^-\pi^+\chi_{c1}$ decay Dalitz plot. The solid (dashed) lines delimit the four vertical (three horizontal) slices that are used to present the fit results in subsequent figures. The coordinates of the vertical (horizontal) lines are $M^2(K^-\pi^+) = 1.00 \text{ GeV}^2/c^4$, $1.75 \text{ GeV}^2/c^4$ and $2.37 \text{ GeV}^2/c^4$ ($M^2(\pi^+\chi_{c1}) = 16.0 \text{ GeV}^2/c^4$ and $19.3 \text{ GeV}^2/c^4$).

are shown in Fig. 7, where the influence of the structure in the $\pi^+\chi_{c1}$ channel is most clearly seen in the second vertical slice. The mass and width of the Z^+ found from the fit are $M = (4150_{-16}^{+31}) \text{ MeV}/c^2$ and $\Gamma = (352_{-43}^{+99}) \text{ MeV}$; the fit fraction of Z^+ events, defined as the integral of the Z^+ contribution over the Dalitz plot divided by the integral of the signal function, $\frac{\int |A_Z|^2 ds_x ds_y}{\int S ds_x ds_y}$, is $(33.1_{-5.8}^{+8.7})\%$. All quoted uncertainties are statistical.

The fit fraction is not determined directly from the fit and its statistical uncertainty is difficult to estimate based on the statistical uncertainties of fit parameters. In this paper the statistical uncertainties of fit fractions are determined using 1000 toy Monte Carlo samples. Each sample is generated according to the probability distri-

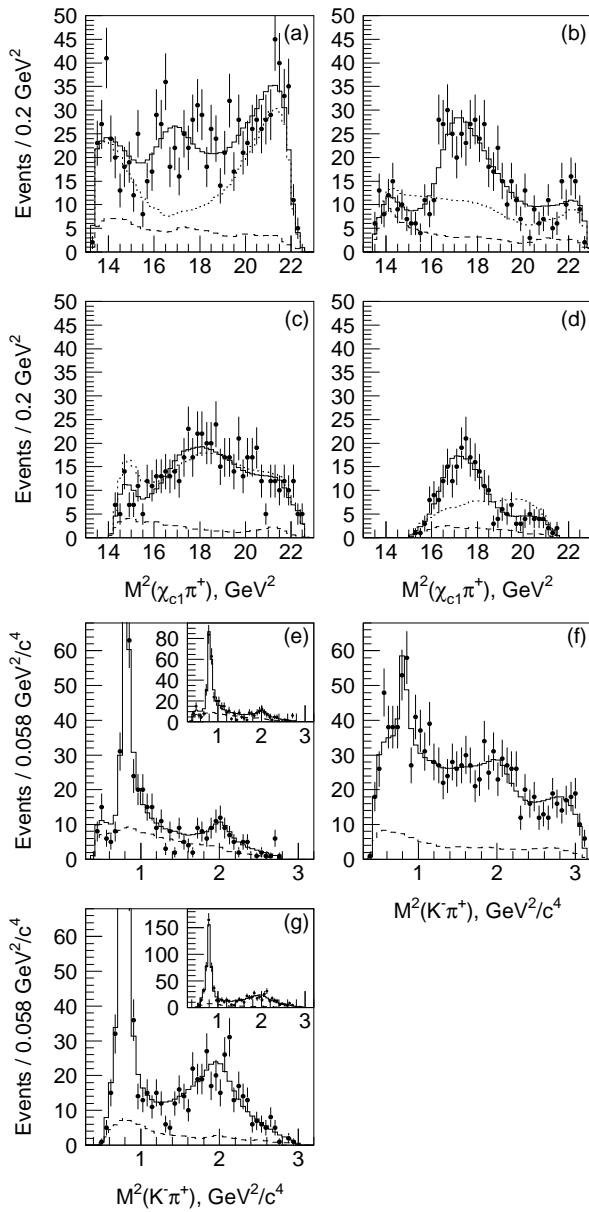


FIG. 7: Dalitz plot fit with the default model, including one Z^+ . Projections for the slices defined in Fig. 6 are shown: (a)-(d) correspond to vertical slices from left to right, (e)-(g) correspond to horizontal slices from bottom to top; in (e) and (g), plots including the full vertical scale are shown inset. The dots with error bars represent data, the solid histograms are the fit results, the dashed histograms represent the background, and the dotted histograms in (a)-(d) represent the sum of all fit components except the Z^+ . The fitting model includes all known K^* resonances and one Z^+ term.

tribution determined from the fit to experimental data, and contains the same number of events as the data. We generate 1000 such samples, fit them, and determine the fit fractions. We fit the distribution of the obtained fit fractions to an asymmetric Gaussian function and consider the sigmas of the Gaussian function as the statistical un-

certainty in the fit fraction.

The significance of the Z^+ , calculated from the difference in log likelihood between fits with and without the Z^+ contribution with the change in the number of degrees of freedom taken into account, is 10.7σ . The results of the fit with the Z^+ contribution excluded from the default fit function are presented in Fig. 8. The fit

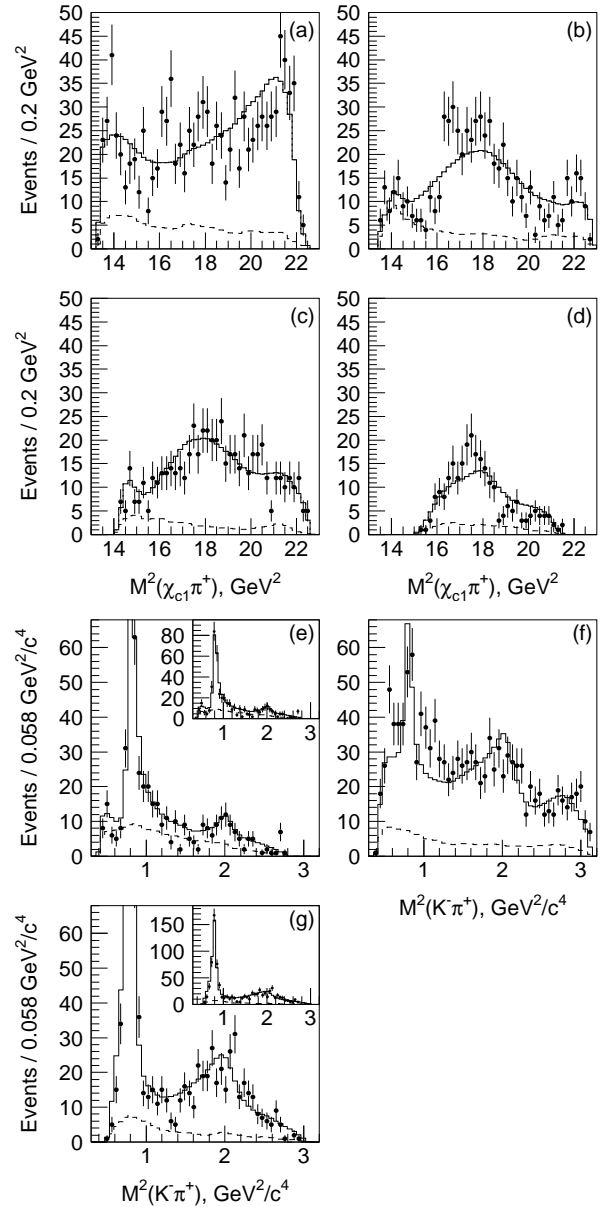


FIG. 8: Dalitz plot fit without any Z^+ term. Projections are shown in (a)-(g) as described for Fig. 7. The dots with error bars represent data, the solid histograms are the fit results, and the dashed histograms represent the background. Here the fitting model with all known K^* resonances and no resonance in the $\pi^+\chi_{c1}$ channel is used.

fractions and significances for each of the resonances included in the default model are listed in Table I.

To study the model dependence, we consider a variety

TABLE I: The fit fractions and significances of all contributions for the fit models with a default set of $K^- \pi^+$ resonances and one Z^+ or two Z^+ resonances.

Contribution	One Z^+		Two Z^+	
	Fit fraction	Significance	Fit fraction	Significance
$Z_{(1)}^+$	$(33.1^{+8.7}_{-5.8})\%$	10.7σ	$(8.0^{+3.8}_{-2.2})\%$	5.7σ
Z_2^+	–	–	$(10.4^{+6.1}_{-2.3})\%$	5.7σ
κ	$(1.9 \pm 1.8)\%$	2.1σ	$(3.6 \pm 2.6)\%$	3.5σ
$K^*(892)$	$(28.5 \pm 2.1)\%$	10.6σ	$(30.1 \pm 2.3)\%$	9.8σ
$K^*(1410)$	$(3.6 \pm 4.4)\%$	1.3σ	$(4.4 \pm 4.3)\%$	2.0σ
$K_0^*(1430)$	$(22.4 \pm 5.8)\%$	3.4σ	$(18.6 \pm 5.0)\%$	4.5σ
$K_2^*(1430)$	$(8.4 \pm 2.7)\%$	5.2σ	$(6.1 \pm 2.9)\%$	5.4σ
$K^*(1680)$	$(5.2 \pm 3.7)\%$	2.2σ	$(4.4 \pm 3.1)\%$	2.4σ
$K_3^*(1780)$	$(7.4 \pm 3.0)\%$	3.6σ	$(7.2 \pm 2.9)\%$	3.8σ

of other fit hypotheses. The results are summarized in Table II. The first row in Table II corresponds to the fit model with the default set of $K^- \pi^+$ resonances. Rows 2 through 6 indicate the results from models in which one of the $K\pi$ resonances: κ , $K^*(1410)$, $K_0^*(1430)$, $K^*(1680)$ or $K_3^*(1780)$, respectively, is removed. Row 7 shows the results when a non-resonant $\chi_{c1} K^-$ amplitude, parameterized as $a e^{ib} e^{-cM(\chi_{c1} K^-)}$, where a , b and c are free parameters, is added to the fit model. This amplitude can be related to a decay that proceeds via a virtual B^* . Rows 8 through 10 show results from fits that include the non-resonant contribution, but without the $K^*(1410)$, $K^*(1680)$ or $K_3^*(1780)$, respectively. Row 11 corresponds to a fit that includes the non-resonant term and releases the experimental constraints on the mass and width of the κ . We also consider models that include the non-resonant contribution, plus an additional $J = 1$ (row 12) or $J = 2$ (row 13) K^* resonance with floating mass and width. Finally, we replaced the κ and $K_0^*(1430)$ contributions with the S -wave component parameterization suggested by the LASS experiment [9] (row 14). We used the following form of the LASS parameterization [10]:

$$A_0 = F_B^{(1)} \cdot \frac{p_B}{m_B} \cdot \left(\frac{\sqrt{s}}{p(\cot \delta - i)} + e^{2i\delta} \frac{m_0^2 \Gamma_0 / p_0}{m_0^2 - s - i m_0 \Gamma_0 \frac{p}{p_0} \frac{m_0}{\sqrt{s}}} \right). \quad (9)$$

Here s is the four-momentum-squared of the $K^- \pi^+$ pair, p is the K^- momentum in the $K^- \pi^+$ c.m. frame, m_0 is the mass and Γ_0 is the width of the $K_0^*(1430)$, p_0 is the K^- momentum calculated for the pole mass of the $K_0^*(1430)$, and the phase δ is determined from the equation $\cot \delta = \frac{1}{ap} + \frac{bp}{2}$, where a , b are the model parameters. We used the LASS optimal values for the a and b [10].

For each fit model the Z^+ significance is estimated. The minimal significance of 6.2σ corresponds to fit model 13 and is considered as the Z^+ significance with systematics taken into account. The fit result for model 13

without the contribution of the Z^+ is shown in Fig. 9. For models with an additional $J = 1$ or $J = 2$ K^* resonance with floating mass and width, the resulting fitted masses and widths of the additional K^* resonances ($M = 2.14 \text{ GeV}/c^2$, $\Gamma = 3.0 \text{ GeV}$ for $J = 1$ and $M = 1.05 \text{ GeV}/c^2$, $\Gamma = 0.26 \text{ GeV}$ for $J = 2$) do not match those of any known $K\pi$ resonance [6].

In the fits described above, the spin of the Z^+ is assumed to be 0. We find that the $J = 1$ assumption does not significantly improve the fit quality (in the default fit model, $-2 \ln L$ changes from 17640.7 to 17638.3 for four additional degrees of freedom).

It is not possible to distinguish the contributions of χ_{c1} helicity $+1$ and -1 in models where the spin of Z^+ is zero. Fits that include both have nearly the same likelihood value as fits with only one.

To address the question of fit quality we constructed a two-dimensional histogram with varying bin sizes, in which there are a minimum of 16 expected events in each bin (95 bins in total). A χ^2 is determined for this histogram, $\chi^2 = \sum_i (n_i - f_i)^2 / f_i$, where n_i is the number of events and f_i is the expectation value for the i -th bin, and a toy MC is used to determine its confidence level. For the fit model with the default set of the $K^- \pi^+$ resonances and one Z^+ resonance (Fig. 7) the confidence level is 0.5%. Such a low confidence level value indicates that the shape of the structure is not well reproduced by a single Breit-Wigner. (The confidence levels of the fits without a Z^+ resonance, shown in Figs 8 and 9, are 3×10^{-10} and 9×10^{-4} , respectively.)

TWO Z^+ 'S?

In the Dalitz plot projections for the first and second vertical slices (*cf.* the top two panels of Fig. 7) the $M(\chi_{c1} \pi^+)$ structure has a doubly peaked shape. This motivated us to add a second Z^+ resonance to the default fit model. The results of the fit with this model are

TABLE II: Different fit models that are used to study systematic uncertainties and the significances of the single- and double- Z^+ hypotheses.

Model	Significance of one Z^+	One Z^+ vs. two Z^+	Significance of two Z^+
1 default (see text)	10.7σ	5.7σ	13.2σ
2 no κ	15.6σ	5.0σ	16.6σ
3 no $K^*(1410)$	13.4σ	5.4σ	14.8σ
4 no $K_0^*(1430)$	10.4σ	5.2σ	14.4σ
5 no $K^*(1680)$	13.3σ	5.6σ	14.8σ
6 no $K_3^*(1780)$	12.9σ	5.6σ	14.4σ
7 add non-resonant $\chi_{c1}K^-$ term	9.0σ	5.3σ	10.3σ
8 add non-resonant $\chi_{c1}K^-$ term, no $K^*(1410)$	11.3σ	5.1σ	13.5σ
9 add non-resonant $\chi_{c1}K^-$ term, no $K^*(1680)$	11.4σ	5.3σ	13.7σ
10 add non-resonant $\chi_{c1}K^-$ term, no $K_3^*(1780)$	10.8σ	5.4σ	13.2σ
11 add non-resonant $\chi_{c1}K^-$ term, release constraints on κ mass & width	9.5σ	5.3σ	10.7σ
12 add non-resonant $\chi_{c1}K^-$ term, new $K^*(J=1)$	7.7σ	5.4σ	9.2σ
13 add non-resonant $\chi_{c1}K^-$ term, new $K^*(J=2)$	6.2σ	5.6σ	8.1σ
14 LASS parameterization of S-wave component	12.4σ	5.3σ	13.8σ

presented in Fig. 10.

The confidence level for this fit, calculated using the method used for the one Z^+ hypothesis, is 42%. A comparison of the likelihood values for the one- and two- Z^+ fits favors the two- Z^+ resonances hypothesis over the one- Z^+ resonance scenario at the 5.7σ level. The masses and widths of the two Z^+ resonances found from the two- Z^+ fit are

$$\begin{aligned}
M_1 &= (4051 \pm 14_{-41}^{+20}) \text{ MeV}/c^2, \\
\Gamma_1 &= (82_{-17-22}^{+21+47}) \text{ MeV}, \\
M_2 &= (4248_{-29-35}^{+44+180}) \text{ MeV}/c^2, \\
\Gamma_2 &= (177_{-39-61}^{+54+316}) \text{ MeV},
\end{aligned}$$

with fit fractions of $f_1 = (8.0_{-2.2-4.2}^{+3.8+9.5})\%$ and $f_2 = (10.4_{-2.3-0.7}^{+6.1+51.5})\%$. The corresponding product branching fractions, calculated as $\mathcal{B}(\bar{B}^0 \rightarrow K^- \pi^+ \chi_{c1}) \times f_{1,2}$, are

$$\begin{aligned}
\mathcal{B}(\bar{B}^0 \rightarrow K^- Z_1^+) \times \mathcal{B}(Z_1^+ \rightarrow \pi^+ \chi_{c1}) &= \\
& (3.0_{-0.8-1.6}^{+1.5+3.7}) \times 10^{-5}, \\
\mathcal{B}(\bar{B}^0 \rightarrow K^- Z_2^+) \times \mathcal{B}(Z_2^+ \rightarrow \pi^+ \chi_{c1}) &= \\
& (4.0_{-0.9-0.5}^{+2.3+19.7}) \times 10^{-5}.
\end{aligned}$$

The product branching fractions are comparable to those of the $Z(4430)^+$ and other charmonium-like states in a leading decay mode [1, 6]. The fit fractions and significances for each of the resonances included in the model are listed in Table I. We find that the phase difference between the two Z^+ resonances is close to $\pi/2$: $\phi_{Z_2^+} - \phi_{Z_1^+} = 1.7_{-0.3}^{+0.2}$.

To estimate systematic errors, we use the models listed in Table II, with two Z^+ resonances instead of one, and

consider the maximum variations of the Z_1^+ and Z_2^+ masses, widths and fit fractions for different fit models as a systematic uncertainty. These uncertainties are given in the first row of Table III.

The possibility of multiple minima can be an issue for complicated fit models with many contributions. In light of this we randomly generated the initial values for the fit parameters and repeated each fit several times. The deepest minimum is selected. (This approach is used also for the single- Z^+ models.) If any secondary minima are within $|\delta(2 \ln L)| < 2$ of the selected solution, they are included in the systematic uncertainty determination.

We also study the systematics due to the uncertainty in the form factors for the decays. In addition to the default value of the r parameter in the Blatt-Weisskopf parameterization $r = 1.6 \text{ GeV}^{-1}$, we also consider $r = 1.0 \text{ GeV}^{-1}$ and $r = 2.0 \text{ GeV}^{-1}$. The variation of the Z^+ parameters is negligible. In addition, we change the assumption about the value of the \bar{B}^0 decay orbital angular momentum for those cases where several possibilities exist, as discussed above. The resulting uncertainties are given in the second row of Table III.

In the phase-space MC, the angular distributions of the $\chi_{c1} \rightarrow J/\psi \gamma$ and $J/\psi \rightarrow \ell^+ \ell^-$ decays are assumed to be uniform. To check the sensitivity of our results to this assumption, we weight the MC events according to the expectations for the χ_{c1} with zero helicity: $1 + 2 \cos^2 \theta_{\chi_{c1}} \cos^2 \theta_{J/\psi} - \cos^2 \theta_{J/\psi}$ [11]. The variation of the Z^+ parameters is found to be negligible.

We estimate systematic errors associated with the event selection by repeating the analysis while loosening the selection requirements on $M(J/\psi \gamma)$, M_{bc} and track quality until the background level is *increased* by a factor of two, and while tightening them until the background

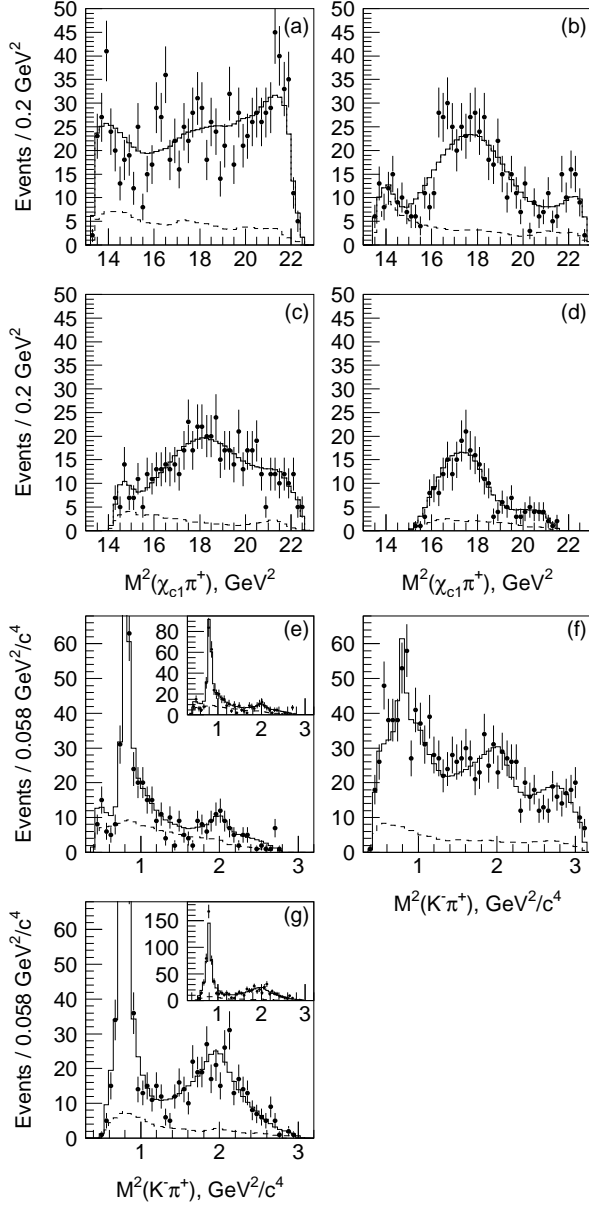


FIG. 9: An alternative Dalitz plot fit without any Z^+ term. Projections are shown in (a)-(g) as described for Figs 7 and 8; point- and line-styles match those from Fig. 8. The fit model with all known K^* resonances, a $\chi_{c1}K^-$ non-resonant contribution, and a new K_2^* , but without a Z^+ term, is used.

level is *decreased* by a factor of two compared to the nominal level. The systematic uncertainties estimated in this way are given in the third row of Table III.

In the fits described above, the spins of both Z^+ resonances are assumed to be zero. We find that a $J = 1$ assumption for either or both does not significantly improve the fit quality, as shown in Table IV, where we show results for all four possible combinations of spin $J = 0$ or $J = 1$ assignment. The variations in the Z_1^+ and Z_2^+ parameters for the different spin assignments are

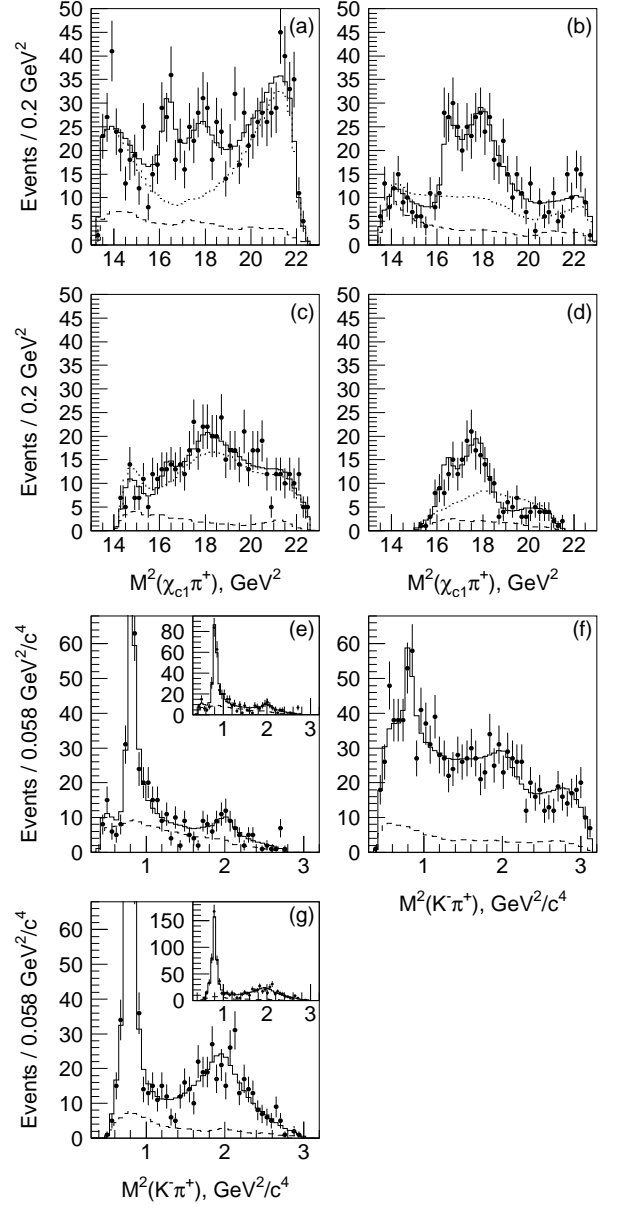


FIG. 10: Dalitz plot fit including two Z^+ terms. Projections are shown in (a)-(g) as described for Fig. 7; point- and line-styles also match those of that figure. The fit model with all known K^* resonances and two Z^+ terms (Z_1^+ , Z_2^+) is used.

considered as systematic uncertainties and are listed in the fourth row in Table III.

To obtain the total systematic uncertainties, the values given in Table III are added in quadrature.

In the extreme case, *i.e.* model 2 where the κ is eliminated, the two-resonance hypothesis is favored over the one-resonance hypothesis with a 5.0σ significance. The hypothesis with two Z^+ resonances is favored over the hypothesis with no Z^+ resonances by at least an 8.1σ level for all models.

We cross-check the estimated significances using toy

TABLE III: Systematic uncertainties in the Z^+ mass, width and fit fraction due to fit model, uncertainty in the form factors, uncertainty in the χ_{c1} , J/ψ decay angular distributions and variation of selection requirements.

	$M_1, \text{MeV}/c^2$	Γ_1, MeV	$f_1, \%$	$M_2, \text{MeV}/c^2$	Γ_2, MeV	$f_2, \%$
Fit model	+18 -18	+15 - 9	+4.6 -3.0	+27 -32	+97 -34	+18.5 - 0.7
Formalism	+3 -0	+8 -0	+0.4 - 0	+ 0 -10	+ 5 -11	+2.5 - 0
Selection	+ 0 -21	+14 - 0	+2.4 -1.4	+87 - 0	+87 - 0	+6.1 - 0
Spin assignment	+ 7 -30	+42 -20	+8.0 -2.6	+156 - 10	+288 - 50	+47.6 - 0

TABLE IV: The $-2\ln L$ values and the change in the number of degrees of freedom for the fits with different spin assignments for the Z_1^+ and Z_2^+ .

J_1	J_2	$-2\ln L$	$\Delta d.o.f.$
0	0	17599.2	0
0	1	17594.3	4
1	0	17597.5	4
1	1	17590.1	8

MC. We generated three types of toy MC events according to the fit results of the fit model with the default set of $K^-\pi^+$ resonances and with either zero, one or two Z^+ resonances (100 samples of each type). We perform the fits to these toy MC samples using the same three fit models. The results (mean and r.m.s.) for the significance of the single Z^+ resonance, the level at which the two-resonance hypothesis is favored over the one-resonance hypothesis and the significance of two resonances compared to the no-resonance hypothesis for all nine combinations are given in Table V. We find that the pattern

TABLE V: A comparison of the zero, one and two Z^+ resonance hypothesis for the toy MC samples generated for 0, 1 and 2 Z^+ resonances. The corresponding significances seen in the data are given for comparison.

Hypotheses compared	Toy MC samples			Data
	0	1	2	
1 over 0	$(1.0 \pm 0.8) \sigma$	$(9.1 \pm 1.0) \sigma$	$(9.4 \pm 0.9) \sigma$	10.7σ
2 over 1	$(2.0 \pm 1.2) \sigma$	$(1.3 \pm 0.8) \sigma$	$(5.4 \pm 1.0) \sigma$	5.7σ
2 over 0	$(1.8 \pm 0.9) \sigma$	$(8.8 \pm 1.0) \sigma$	$(10.9 \pm 1.4) \sigma$	13.2σ

of the significances observed in data is reproduced well by the toy MC with two Z^+ resonances.

BRANCHING FRACTION OF THE $\bar{B}^0 \rightarrow K^*(892)^0 \chi_{c1}$ DECAY

From the K^* fit fraction from the two- Z^+ fit given in Table I, we determine the branching fraction

$\mathcal{B}(\bar{B}^0 \rightarrow K^*(892)^0 \chi_{c1}) = (1.73_{-0.12}^{+0.15+0.34}) \times 10^{-4}$. The systematic uncertainty is estimated in the same way as described above for the $Z_{1,2}^+$ parameters. The result is significantly below the current world average $(3.2 \pm 0.6) \times 10^{-4}$ [6]. However, this is the first measurement of the branching fraction that takes into account interference with other decay channels that produce the same final state. The fraction of longitudinal polarization is found to be $(94.7_{-4.8-9.9}^{+3.8+4.6})\%$, which confirms the conclusion that the $B \rightarrow K^*(892)\chi_{c1}$ decay is dominated by longitudinal polarization [12, 13]. The significances of other intermediate K^* resonances are below the 5σ level when systematic uncertainties from various fit models are taken into account.

ANGULAR DISTRIBUTIONS OF THE χ_{c1} AND J/ψ DECAYS

Angular distributions for $\chi_{c1} \rightarrow J/\psi\gamma$ and $J/\psi \rightarrow \ell^+\ell^-$ decays are not used in the Dalitz analysis and therefore provide a useful cross-check. For the χ_{c1} in the helicity zero state the expected angular distribution for $\chi_{c1} \rightarrow J/\psi\gamma$ and $J/\psi \rightarrow \ell^+\ell^-$ decay is $P_0 = \frac{9}{32}(1 + 2\cos^2\theta_{\chi_{c1}}\cos^2\theta_{J/\psi} - \cos^2\theta_{J/\psi})$, while for the χ_{c1} in the helicity ± 1 state the expected angular distribution is $P_{\pm 1} = \frac{9}{32}(1 - \cos^2\theta_{\chi_{c1}}\cos^2\theta_{J/\psi})$. Here it is assumed that different J/ψ helicity states do not interfere. We integrate the helicity zero and helicity ± 1 components of the fit function over the Dalitz plot and find the relative contributions w_0 and $w_{\pm 1}$. The expected angular distribution is then $P = w_0 P_0 + w_{\pm 1} P_{\pm 1}$.

The $\cos\theta_{\chi_{c1}}$ and $\cos\theta_{J/\psi}$ distributions for the entire Dalitz plot, are presented in Fig. 11; for the leftmost vertical slice containing the $K^*(892)$ signal in Fig. 12; and for the middle horizontal slice dominated by the Z^+ resonances in Fig. 13. The agreement with predictions is good. It is evident that the different models give very similar predictions and these angular distributions are not useful for discriminating between them.

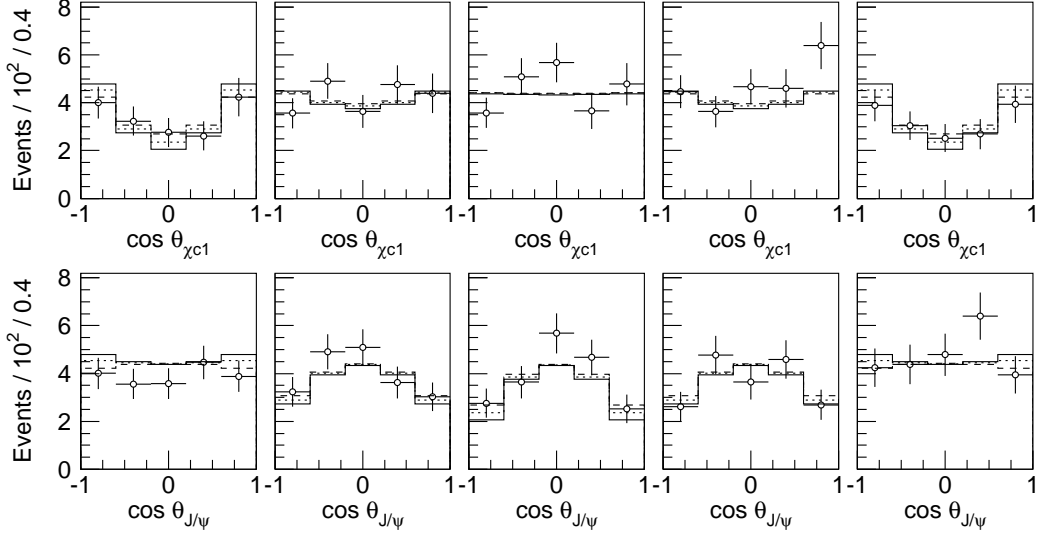


FIG. 11: $\cos\theta_{\chi_{c1}} (\cos\theta_{J/\psi})$ distributions in $\cos\theta_{J/\psi} (\cos\theta_{\chi_{c1}})$ bins for the entire Dalitz plot. The dots with error bars are data, the solid (dashed) histograms are the predictions of the model with two $J = 0$ ($J = 1$) Z^+ resonances, the dotted histograms are the predictions of the model with no Z^+ . The $\cos\theta_{J/\psi} (\cos\theta_{\chi_{c1}})$ bins are $(-1, -0.6)$, $(-0.6, -0.2)$, $(-0.2, 0.2)$, $(0.2, 0.6)$ and $(0.6, 1)$.

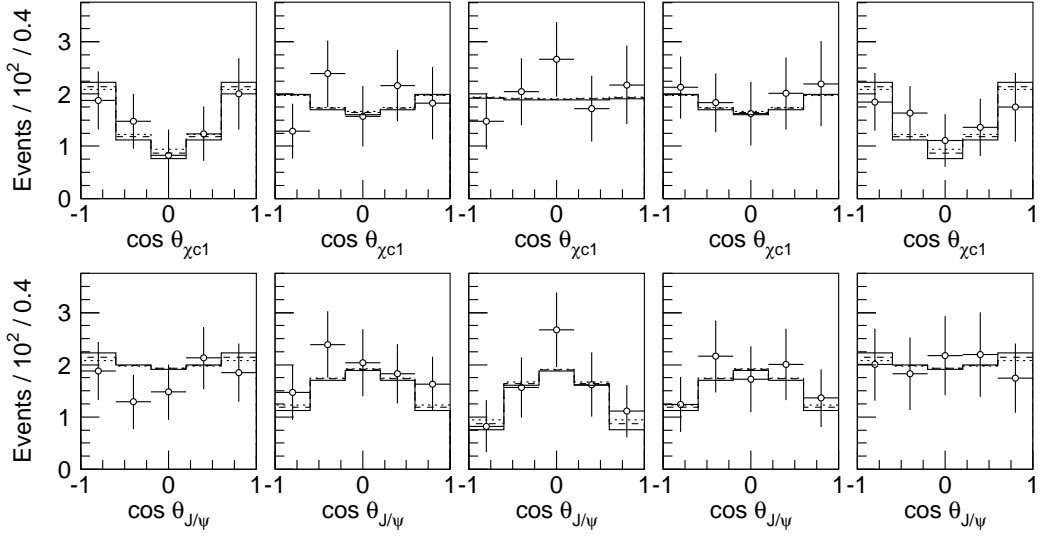


FIG. 12: $\cos\theta_{\chi_{c1}} (\cos\theta_{J/\psi})$ distributions in $\cos\theta_{J/\psi} (\cos\theta_{\chi_{c1}})$ bins for the vertical Dalitz plot slice that contains the $K^*(892)$ signal. The dots with error bars are data, the solid (dashed) histograms are the predictions of the model with two $J = 0$ ($J = 1$) Z^+ resonances, the dotted histograms are the predictions of the model with no Z^+ . The $\cos\theta_{J/\psi} (\cos\theta_{\chi_{c1}})$ bins are $(-1, -0.6)$, $(-0.6, -0.2)$, $(-0.2, 0.2)$, $(0.2, 0.6)$ and $(0.6, 1)$.

CONCLUSIONS

A broad doubly peaked structure is observed in the $\pi^+\chi_{c1}$ invariant mass distribution in exclusive $\bar{B}^0 \rightarrow K^-\pi^+\chi_{c1}$ decays. When fitted with two Breit-Wigner

resonance amplitudes, the resonance parameters are

$$M_1 = (4051 \pm 14_{-41}^{+20}) \text{ MeV}/c^2,$$

$$\Gamma_1 = (82_{-17}^{+21+47}) \text{ MeV},$$

$$M_2 = (4248_{-29}^{+44+180} -_{35}) \text{ MeV}/c^2,$$

$$\Gamma_2 = (177_{-39}^{+54+316} -_{61}) \text{ MeV},$$

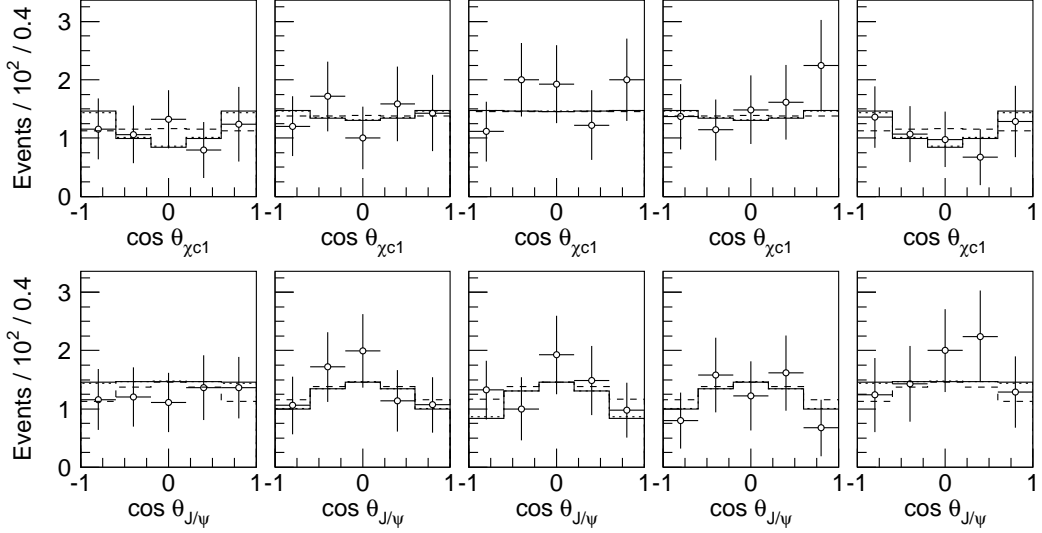


FIG. 13: $\cos\theta_{\chi_{c1}}$ ($\cos\theta_{J/\psi}$) distributions in $\cos\theta_{J/\psi}$ ($\cos\theta_{\chi_{c1}}$) bins for the horizontal slice of the Dalitz plot that contains the $Z_{1,2}^+$ signals. The dots with error bars are data, the solid (dashed) histograms are the predictions of the model with two $J = 0$ ($J = 1$) Z^+ resonances, the dotted histograms are the predictions of the model with no Z^+ . The $\cos\theta_{J/\psi}$ ($\cos\theta_{\chi_{c1}}$) bins are $(-1, -0.6)$, $(-0.6, -0.2)$, $(-0.2, 0.2)$, $(0.2, 0.6)$ and $(0.6, 1)$.

with the product branching fractions of

$$\begin{aligned} \mathcal{B}(\bar{B}^0 \rightarrow K^- Z_1^+) \times \mathcal{B}(Z_1^+ \rightarrow \pi^+ \chi_{c1}) &= \\ & (3.0^{+1.5+3.7}_{-0.8-1.6}) \times 10^{-5}, \\ \mathcal{B}(\bar{B}^0 \rightarrow K^- Z_2^+) \times \mathcal{B}(Z_2^+ \rightarrow \pi^+ \chi_{c1}) &= \\ & (4.0^{+2.3+19.7}_{-0.9-0.5}) \times 10^{-5}. \end{aligned}$$

The invariant mass distribution $M(\chi_{c1}\pi^+)$ for the Dalitz plot slice $1.0 \text{ GeV}^2/c^4 < M^2(K^-\pi^+) < 1.75 \text{ GeV}^2/c^4$, where the contribution of the structure in the $\pi^+\chi_{c1}$ channel is most clearly seen, is shown in Fig. 14.

Recently Belle observed the first candidate for a charmonium-like state with non-zero electric charge, the $Z(4430)^+$ [1]. The two resonance-like structures reported here represent additional candidate states of similar character. The existence of new resonances decaying into $\chi_{cJ}\pi$ is expected within the framework of the hadro-charmonium model [14].

In addition, we measure the branching fractions $\mathcal{B}(\bar{B}^0 \rightarrow K^-\pi^+\chi_{c1}) = (3.83 \pm 0.10 \pm 0.39) \times 10^{-4}$ and $\mathcal{B}(\bar{B}^0 \rightarrow K^*(892)^0\chi_{c1}) = (1.73^{+0.15+0.34}_{-0.12-0.22}) \times 10^{-4}$.

Acknowledgments

We thank the KEKB group for the excellent operation of the accelerator, the KEK cryogenics group for the efficient operation of the solenoid, and the KEK computer group and the National Institute of Informatics for valuable computing and SINET3 network support. We acknowledge support from the Ministry of Education, Culture, Sports, Science, and Technology of Japan and the Japan Society for the Promotion of Science;

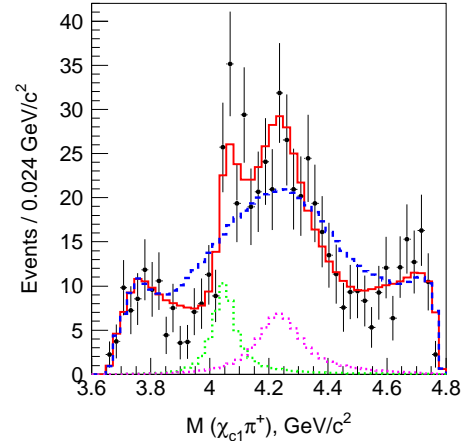


FIG. 14: The $M(\chi_{c1}\pi^+)$ distribution for the Dalitz plot slice $1.0 \text{ GeV}^2/c^4 < M^2(K^-\pi^+) < 1.75 \text{ GeV}^2/c^4$. The dots with error bars represent data, the solid (dashed) histogram is the Dalitz plot fit result for the fit model with all known K^* and two (without any) $\chi_{c1}\pi^+$ resonances, the dotted histograms represent the contribution of the two $\chi_{c1}\pi^+$ resonances.

the Australian Research Council and the Australian Department of Education, Science and Training; the National Natural Science Foundation of China under contract No. 10575109 and 10775142; the Department of Science and Technology of India; the BK21 program of the Ministry of Education of Korea, the CHEP SRC program and Basic Research program (grant No. R01-2005-000-10089-0) of the Korea Science and Engineering Foundation, and the Pure Basic Research Group program of the

Korea Research Foundation; the Polish State Committee for Scientific Research; the Ministry of Education and Science of the Russian Federation and the Russian Federal Agency for Atomic Energy; the Slovenian Research Agency; the Swiss National Science Foundation; the National Science Council and the Ministry of Education of Taiwan; and the U.S. Department of Energy.

-
- [1] S.-K. Choi *et al.* (Belle Collaboration), Phys. Rev. Lett. **100**, 142001 (2008).
- [2] S. Kurokawa and E. Kikutani, Nucl. Instrum. Methods Phys. Res., Sect. A **479**, 117 (2002), and other papers included in this volume.
- [3] A. Abashian *et al.* (Belle Collaboration), Nucl. Instrum. Methods Phys. Res., Sect. A **479**, 117 (2002).
- [4] Z. Natkaniec *et al.* (Belle SVD2 Group), Nucl. Instrum. Methods Phys. Res. Sect. A **560**, 1 (2006).
- [5] R. Brun *et al.*, GEANT 3.21, CERN DD/EE/84-1, 1984.
- [6] W.-M. Yao *et al.* (Particle Data Group), J. Phys. G **33**, 1 (2006).
- [7] S. Kopp *et al.* (CLEO Collaboration), Phys. Rev. D **63**, 092001 (2001).
- [8] J. Blatt and V. Weisskopf, Theoretical Nuclear Physics, p.361, New York: John Wiley & Sons (1952).
- [9] D. Aston *et al.* (LASS Collaboration), Nucl. Phys. B **296**, 493 (1988).
- [10] B. Aubert *et al.* (BABAR Collaboration), Phys. Rev. D **72**, 072003 (2005) [Erratum-ibid. D **74**, 099903 (2006)].
- [11] The $\chi_{c1} \rightarrow J/\psi\gamma$ decay is governed by two helicity amplitudes, $H_{1,1}^{\chi_{c1}}$ and $H_{0,1}^{\chi_{c1}}$, where the first and second subscripts correspond to the helicity of the J/ψ and γ , respectively. Both experimental results and theoretical calculations indicate that the quadrupole contribution to the $\chi_{c1} \rightarrow J/\psi\gamma$ transition is small, and therefore $|H_{1,1}^{\chi_{c1}}| \simeq |H_{0,1}^{\chi_{c1}}|$.
- [12] C. Baglin *et al.* (R704 Collaboration), Phys. Lett. B **195**, 85 (1987); K. J. Sebastian, H. Grotch and F. L. Ridener, Phys. Rev. D **45**, 3163 (1992).
- [13] N. Soni *et al.* (Belle Collaboration), Phys. Lett. B **634**, 155 (2006).
- [14] B. Aubert *et al.* (BABAR Collaboration), Phys. Rev. D **76**, 031102 (2007).
- [15] S. Dubynskiy and M. B. Voloshin, arXiv:0803.2224 [hep-ph].